Full Length Article

Engineered SnO$_2$-based thin films for efficient CO$_2$ gas sensing at room temperature

Eleonora Bolli [a,*], Alessandro Bellucci [a], Matteo Mastellone [b], Alessio Mezzi [c], Stefano Orlando [b], Riccardo Polini [d], Raffaella Salerno [d], Antonio Santagata [b], Veronica Valentini [a], Daniele Maria Trucchi [a]

[a] DiaTHEMA Lab, Institute of Structure of Matter (CNR-ISM), U.O.S. Montelibretti, Via Salaria km 29.300, 00015 Monterotondo, Italy
[b] FemtoLAB, Institute of Structure of Matter (CNR-ISM), U.O.S. Tito Scalo, Zona Industriale, 85050 Tito, Italy
[c] EscaLab, Institute for the Study of Nanostructured Materials (CNR-ISMN), Montelibretti, Via Salaria km 29.300, 00015 Monterotondo, Italy
[d] Dipartimento di Scienze e Tecnologie Chimiche, Università degli Studi di Roma Tor Vergata, Via della Ricerca Scientifica, 00133 Rome, Italy

ARTICLE INFO

ABSTRACT

Tin oxide (SnO$_2$)-based thin films were deposited on alumina printed circuit boards via electron beam evaporation to fabricate CO$_2$ gas sensors operating at room temperature. Femtosecond laser surface nanotexturing was applied as a novel approach to optimize key gas sensitivity parameters, including surface roughness and grain size. Raman and X-ray photoelectron spectroscopy revealed that the sensitive layer consists of a 1 μm SnO film with a non-stoichiometric SnO$_2$ upper layer for the as-deposited film. The electronic disparity between these layers forms a native SnO-SnO$_2$ interface, creating a p-n junction that enhances sensor sensitivity. This sensor shows a sensing response ranging from 7 % to 20 % for CO$_2$ concentrations of 1000 to 2000 ppm, and up to 40 % at 5000 ppm. Laser irradiation introduced periodic surface structures (~ 800 nm), increasing the roughness and the number of active sites for the gas sensing. Although no significant improvements were observed in terms of sensitivity, the fs-laser treated sensor exhibited enhanced stability and reproducibility, indicating its potential for low-energy consumption gas sensing platforms for indoor air quality applications.

1. Introduction

In recent years, the demand for energy-efficient and sensitive gas sensors has increased, driven by the need to monitor environmental and human health [1]. Common air pollutants include particulate matter and gases such as ozone (O$_3$), nitrogen dioxide (NO$_2$), sulphur dioxide (SO$_2$), volatile organic compounds (VOCs), carbon mono/di-oxides (CO, CO$_2$) [2,3].

While monitoring potentially harmful gases in urban areas is essential, it is even more critical in indoor environments such as homes, schools, and offices, where their concentrations can be 2–5 times higher than outdoor levels and people spend approximately 90 % of their time [4].

Among various sensor technologies, Metal Oxide Semiconductor (MOX) gas sensors have garnered significant attention. MOX sensors, a type of chemiresistor, operate by changing their electrical resistance when exposed to a target gas. This easy operating principle enables excellent performance at a low cost. [5,6]. Among the different MOX tested as active sensing material, tin dioxide (SnO$_2$) thin films, in particular, have been extensively researched due to their numerous advantages, including high sensitivity, rapid response and recovery times, cost-effectiveness, and wide availability [7–12]. However, a drawback of SnO$_2$-based sensors is their high operating temperatures, typically between 250–400 °C, required for optimal performance. Operating at such temperatures, especially in real-time gas monitoring, significantly increases energy consumption, complexity of the electronic conditioning, and accelerates device degradation, necessitating frequent maintenance and incurring additional expenses [13–15].

It is reasonable to consider addressing the requirement of operating temperature reduction by enhancing also the sensor's performance in terms of sensitivity and selectivity. To this end, recent research has explored several strategies; first of all, take advantage of the low-dimensional materials properties in order to exploit the excellent surface-volume ratio and maximize the useful surface for the interaction

with the gas [10,16–19]. Another approach involves doping which, contributing to a significant increase in the concentration of oxygen vacancies, increases the active sites where adsorption and reaction with the target gas can occur [20]. Examples of doped SnO_2-based gas sensors operating at RT are recently reported [21–24]. Another strategy involves the use of composite and multilayer materials that form p-n heterojunctions, enhancing charge transfer rates to improve gas sensitivity. Systems incorporating a p-type semiconductor with n-SnO_2 fall into this category, as reported in various studies [25–27]. These structures aim to achieve both low operating temperatures and high performance (e.g., high sensitivity and fast response), although the technological complexity of these approaches makes them challenging to implement on a large scale, leading to a shortage of SnO_2-based systems capable of detecting CO_2 at room temperature. The following Table 1 presents recent SnO_2-based CO_2 sensors, along with their respective operating temperatures.

An innovative solution involves employing femtosecond (fs) laser treatments. These treatments modify the surface morphology by producing well-organized and periodic geometrical features, commonly known as Laser Induced Periodic Surfaces Structures (LIPSS) [40], increasing the surface area-to-volume ratio and reducing the grain size [41,42]. Additionally, fs-laser treatments introduce surface defects and electronically active defect levels in the semiconductor bandgap [43], potentially enhancing the performance of gas sensors. Despite its widespread use to modify wettability, optical and electronical properties of the materials in different scientific fields [43–46], fs-laser treatments have not been studied for enhancing the sensitivity of thin films used as gas sensors. The ultra-short duration of the laser pulse minimizes heat-related damage, preserving the material's integrity. During treatment, rapid material redistribution leads to morphological and electronic changes. The key advantage of these treatments is their reproducibility and efficiency, potentially facilitating their adoption as a standardized industrial process and significantly reducing costs.

The proposed SnO_2-based gas sensor, designed to enhance CO_2 detection at room temperature, was morphologically characterized using scanning electron microscopy (SEM). Surface roughness and area were analysed with atomic force microscopy (AFM). Raman spectroscopy (RS) and X-ray photoelectron spectroscopy (XPS) techniques were employed for structural and elemental analysis. Following this, the thin film was treated with a fs-laser, and its CO_2 gas sensitivity was tested at room temperature.

2. Experimental section

2.1. Films deposition by electron beam evaporation

Thin films of tin oxide were deposited on printed-circuit board (PCB) alumina substrates (thickness: 1 mm, produced by CERcuits BV,Geel, Belgium) using electron beam deposition, starting from SnO_2 pellets (Mateck GmbH, purity 99.95 %) as target materials. The deposition was performed in a high vacuum chamber evacuated to a base pressure of approximately 1 x 10^{-6} mbar. The SnO_2 pellets were held in a Al_2O_3 crucible (Kurt J. Lesker Company GmbH, Dresden, Germany) and evaporated by an electron beam with a kinetic energy of 5.75 keV and a current of 40 mA, controlled through an electromagnetic lens system to ensure a homogeneous deposition process. During deposition, the chamber pressure was maintained at approximately 1 x 10^{-4} mbar. Due to the large roughness of the alumina substrate, a thickness of 1 μm was chosen as the thinnest option, ensuring both complete and uniform coverage. To allow fine control over the process and limited uncontrolled kinetics and poorer quality thin film properties, the e-beam deposition rate was kept to 1 nm/s. Moreover, the thickness of the film was controlled during the deposition through a calibrated quartz microbalance that allowed to accurately deposit the chosen thickness of material, inducing a shutter to close when the nominal thickness of 1 μm was reached. The thickness of the deposited film was then verified by AFM profile analysis. The roughness average (Ra) parameter representing the surface roughness, derived from AFM scans (shown in detail in the next section), was used to quantify the excursion from the thickness across the surface. This procedure leads to the film thickness estimation of 1.000 ± 0.067 μm. Furthermore, as described in detail in the next sections, this film appears to be completely covered by an ultra-thin non-stoichiometric SnO_2 layer (< 10 nm), creating a p-n junction at the interface. The schematic illustration of the sensor is shown in Fig. 1.

2.2. Structure and morphology characterization

The morphology of the SnO-SnO_2 thin films has been investigated by

Table 1
SnO_2-based CO_2 sensors.

| Materials	Method/structure	Operating Temperature (°C)	[CO2] (ppm)	Response/Recovery Times (s)	References	Year
SnO_2	Co-precipitation/ Nanoparticles	240	2000	350/4	[28]	2016
Ni-SnO_2	microwave-irradiation/nanoparticles	275	100	4/-	[22]	2020
8at% LaOCl–SnO_2	Electrospinning/Nanofibers	300	1000	24/92	[29]	2017
SnO_2@ZIF-67	Mixing Core-shell	205	5000	220/25	[30]	2018
$LaFeO_3$–SnO_2	Mixing Porous powders	250	4000	< 20/–	[31]	2017
5 wt%Sn–CdO	Coprecipitating /Nanopowders	250	5000	110/140	[32]	2015
SnO_2@La4at%	Impregnation/Nanoparticles	250/N2	500	20/75	[33]	2014
Sb@SnO_2	sol–gel spin coating/Thin film	30–80	–	<12/<10	[21]	2022
Au@La_2O_3/SnO_2	Electrospinning/ nanofibers	300	100	–	[34]	2020
SnO_2	Co-precipiotation	240	20,000	31/47	[28]	2016
La@SnO_2	Hydrotgermal and impregration /nanoparticles	250	500	30/75	[33]	2014
La@SnO_2	Electrospinning/nanofibers	300	1000	–	[29]	2017
La2O3@SnO_2	MHP/layer	400	1000	–	[36]	2017
Sb@SnO_2	Solution combustion/Nanoparticles	350	1000	–	[37]	2022
Sb@SnO_2	Sol-gel spin coating/Spherical particles	30	–	2.5/5.8	[21]	2022
SnO_2/rGO	Reduction/nanocomposite film	23	5	41/47	[38]	2021
Pt@LaO_3/SnO_2	Screen-printing/thick film	225	1000	–	[39]	2016
Nano-SnO_2	nano-powders annealed/ nanothick-films	23	2000 to 4000	10–350/4–54	[28]	2016
ZnO doped SnO_2 films	spray deposited/ nanocrystalline SnO2 films	270–310	500	40/32	[35]	2017
SnO-SnO2	e-beam/thin films heterojunction	20	110 to 5000	1/120	This work	2024
SnO-SnO2 fs-laser treated	e-beam + fs.laser treatement / thin films + LIPSS	20	110 to 5000	1/-	This work	2024
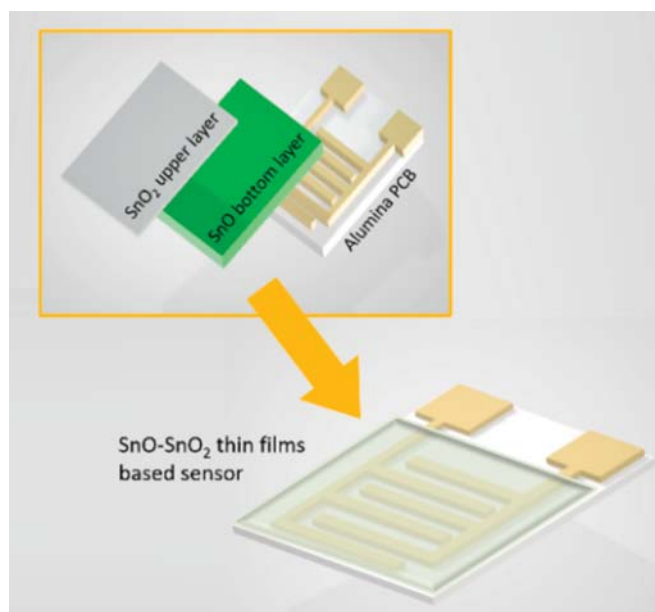
Fig. 1. Schematic illustration of SnO-SnO$_2$ based gas sensor.

Field-Emission Gun Scanning Electron Microscopy (FEG-SEM- Zeiss Leo Supra 35, Germany) and by AFM carried out with use of an OmegaScope platform (HORIBA Ltd., Kyoto, Japan). AFM imaging was performed in tapping mode, setting the operational amplitude at 60 nm, and using a silicon pyramidal tip (MikroMasch HQ:NSC15/Al BS; Wetzlar, Germany) with a characteristic radius of $\sim$ 8 nm. The resonance frequency was 325 kHz. The scan rate was fixed at 0.5 Hz. All the AFM data were acquired, filtered, and analysed using the AIST-NT.v3.5. SPM control software. Raman measurements were carried out using a Horiba Scientific LabRam HR Evolution confocal spectrometer equipped with a 100 mW Oxxius (λ_{exc} = 532 nm) laser source and a computerized XY-table, an electron-multiplier CCD detector, and an Olympus U5RE2 microscope with a 100x objective (laser spot on the sample surface 0.7 μm) with a numerical aperture (NA) of 0.9, and a grating with 1800 grooves/mm were used. All Raman spectra were recorded in backscattering geometry focalizing 10 % of the laser sources power at the sample and ten spectra with an accumulation time of 10 s were averaged. XPS enabled the investigation of the composition of the SnO-SnO$_2$ thin films before and after the fs-laser treatment, and it was carried out by using a spectrometer ESCALAB 250 Xi (Thermo Fisher Scientific Ltd., East Grinstead, UK), equipped with a monochromatic Al Kα source (hν = 1486.6 eV) and a hemispherical analyzer with six-channeltron as the detection system. The XPS measurements were performed operating in an ultra-high vacuum chamber at a base pressure of about 8 $\times$ 10^{-9} mbar. The binding energy (BE) scale was calibrated by positioning the C 1 s adventitious carbon peak at BE = 284.8 eV, with an accuracy of ± 0.1 eV. The spectra were collected and processed by Avantage software v.5.9 (Thermo Fisher Scientific, East Grinstead, UK).

2.3. Laser treatment

The surface nanotexturing process was carried out using a Ti:Sapphire femtosecond laser (Spectra-Physics, Milpitas, CA, USA) with the following characteristics: pulse duration of 100 fs, linear polarization, laser wavelength (λ) of 800 nm, repetition rate of 1 kHz (corresponding to 1 ms of time delay between two generated pulses). The laser beam was generated by a mode-locked oscillator and subsequently regeneratively amplified. The laser impinged the surface following a boustrophedonic movement (i.e., scanning a surface line by line, horizontally from left to right, and then the next line below moving from right to left). This pattern repeats until the entire area is covered (the LIPSS fabrication is

extended to the entire thin film area covering the alumina PCB with deposited area of approximately 20x20 mm^2). This method minimizes the time spent repositioning between lines. Pulses were perpendicularly focused in air by an objective lens (4$\times$, N.A. = 0.10) onto the surface of the thin film. The samples were moved by an automated X-Y translational stage (μFAB Microfabrication Workstation, Newport, CA, USA). The laser spot size was evaluated *a posteriori* through the use of scanning electron microscopy (SEM) following the methodology illustrated in Ref. [47]. The method permits to assess the 1/e^2 Gaussian beam diameter. The estimated diameter is approximately 100 μm.

After preliminary testing, not showed in this paper for the sake of brevity, the laser pulse energy used was 4.5 μJ to obtain regular and homogeneous LIPSS. In scanning mode, the number of overlapping pulses per unit area is controlled by adjusting the scanning speed, denoted as v, following the relationship N = wf/v, where f is the laser repetition rate and w is the laser diameter on the focal spot. The selected scanning speed was 3000 μm/s.

2.4. Gas sensing

The CO$_2$ sensitivity tests were conducted on SnO-SnO$_2$ thin films (the receptor part of the sensor) deposited on an alumina PCB, both before and after fs-laser treatment. The substrate type was selected for microelectronics applications because of its excellent thermal conductivity, mechanical strength, low dielectric constant, and minimal dielectric loss. To transduce the surface interaction of the film with CO$_2$, two copper (Cu, 35 μm) electrodes were deposited onto the substrates with a minimum inter-electrode gap of 10 μm. A dedicated connector was soldered directly to these contacts, facilitating an easy push-and-pull connection to the signal conditioner. The gas sensor tests were conducted in a commercial glove box (Cole-Parmer Instrument Company, LLC, UK) with a volume of approximately 0.25 m^3. The glove box allowed for monitoring and controlling the temperature and humidity throughout the tests, which were maintained at 20 °C and 50 ± 5 %, respectively, to simulate typical comfortable indoor conditions. Additionally, the glove box maintained confined gas concentrations, with various CO$_2$ concentration levels achieved by mixing balanced CO$_2$ with dry air. The methodology for measuring gas sensitivity followed the same procedure as in our previous work [18]. Specifically, thanks to the use of a customized fluxmeter (IONVAC Process srl, Pomezia, Italy), it was possible to regulate the flow of CO$_2$ in the chamber, which was evacuated by a membrane pump (pressure of $\sim$ 10^{-1} mbar) to ensure stable conditions and rapid gas removal. The current measurements were carried out by connecting the sensor to an electrometer (Keithley 487 Picoammeter/Voltage Source), with data recorded automatically through the management of the signals using the GPIB protocol and software specifically developed in LabVIEW (National Instruments, Austin, TX, USA).

3. Results and Discussion

The thin films obtained by electron beam deposition from SnO$_2$ pellets were morphologically characterized using SEM. SEM micrographs show that the alumina's morphology significantly influences the film's morphology. Despite being covered by approximately 1 μm of tin oxides, the large crystalline grains of alumina remain visible (see SEM images, Fig. 2a,b). This makes it difficult to assess the film's uniformity solely from SEM images. The same issue applies to the AFM image (Fig. 2c). Only the higher resolution AFM image provides weak evidence of the presence of the deposited film, showing a rough layer with tiny grains over the alumina (refer to Fig. 2d). AFM analysis was also used to assess surface roughness and estimate the surface area. Hence, the presence of the film is confirmed by changes in roughness parameters and the estimated surface area obtained from the analyses of 15 μm x 15 μm as scanned area and 500 x 500 pixels as lateral resolution images. After film deposition, the roughness values Ra and Rms increased from

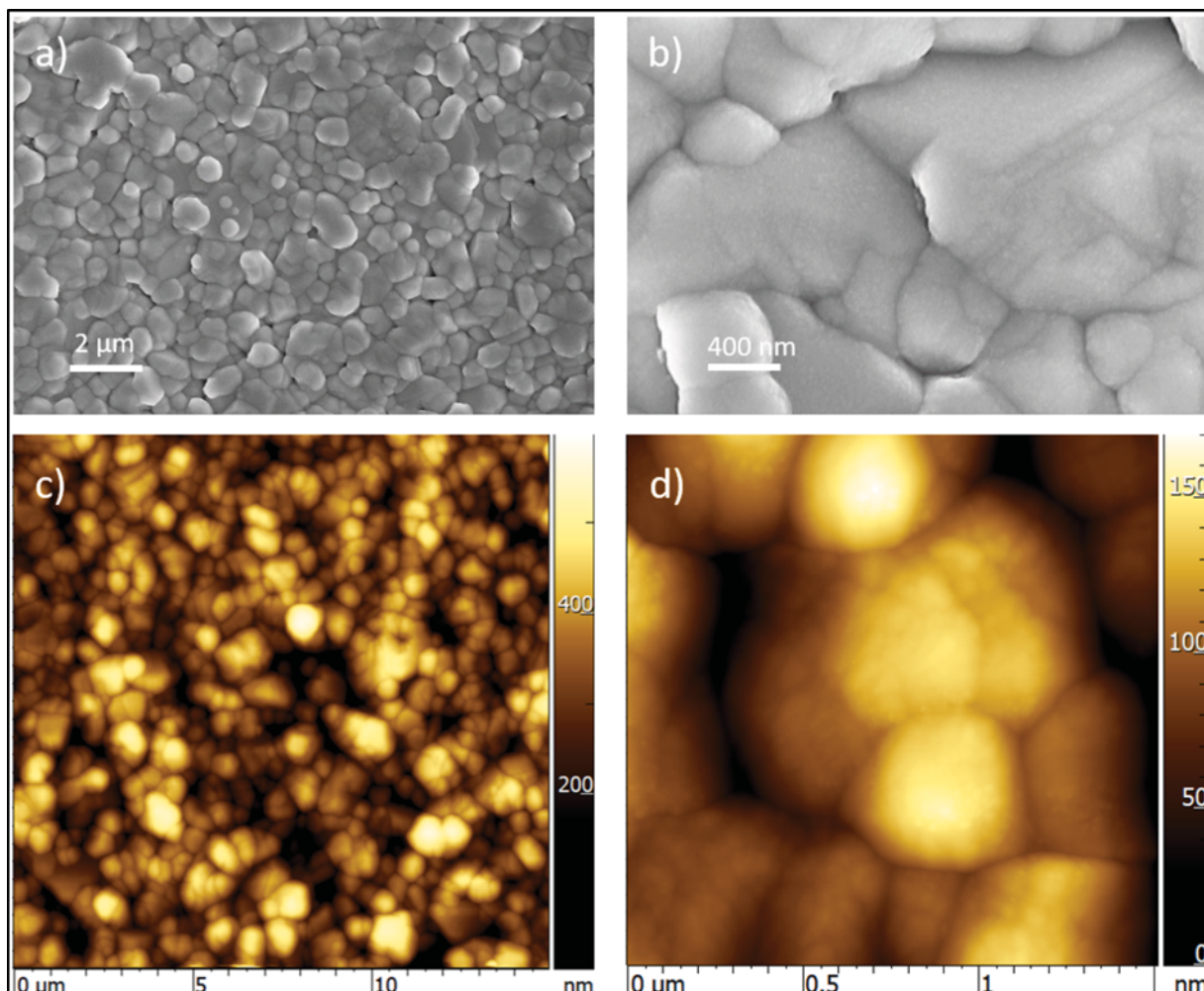**Fig. 2.** SEM micrographs (**a, b**) and AFM topographies (**c,d**) of SnO-SnO$_2$ films as deposited on Al$_2$O$_3$ substrate at different magnifications.

62.3 nm to 67.6 nm and from 78.1 nm to 85.2 nm, respectively. The surface area increased from 231.9 μm^2 to 247.1 μm^2, as reported in Table 2 (the values were estimated by the use of AIST-NT.v3.5. software).

After deposition, the sample was subjected to the fs-laser irradiation. As explained above, the choice to apply fs-laser treatment was driven by its capability to modify surface morphology to induce a texturing of the surface microstructure by creating so-called Laser-Induced Periodic Surface Structures (LIPSS), which increase surface area and provide more active sites for gas adsorption [48]. Additionally, the laser treatment could also change the surface chemistry, by adding oxygen vacancies during localized heating and rapid cooling, which can act as actively site for CO$_2$ adsorption. These phenomena could lead to enhanced electronic properties, such as reduced resistance and improved charge carrier mobility, leading to more intense signal responses and faster reaction times. These mechanisms could be promising

especially for improving the sensor's selectivity and response at RT, overcoming the need for elevated temperatures (300–350 °C) traditionally required by SnO$_2$-based sensors. The morphological alterations are clearly visible under scanning microscopy (see Fig. 3 a,b), which shows the emergence of the LIPSS with a spatial periodicity of $\Lambda = 750$ nm $\pm$ 50 nm, as estimated using the 2D-FFT transformation method. The 2D-FFT transformation of a large-area SEM image (45 μm x 65 μm) and the corresponding intensity signal profile are shown in Fig. 3e and 3f, respectively. This periodicity aligns with the Ti: Sapphire femtosecond laser wavelength used (800 nm), confirming the condition $\Lambda = \lambda_{fs}$, as expected for metals and narrow bandgap semiconductors [49] such as SnO [26,50]. Similarly, roughness and surface area parameters were evaluated through AFM analysis (Fig. 3 c,d). Following laser treatment, the roughness parameters Ra and RMS exhibited significant increases from 67.6 nm to 272.0 nm and from 85.2 nm to 303.0 nm, respectively. Likewise, the surface area value surged from 247.1 μm^2 to 285.1 μm^2. A summary of the comparison between all roughness parameters and surface area values is presented in Table 2.

The Raman and XPS spectrometric analyses provide comprehensive insights into the structure and composition of the as-deposited films. Regarding Raman spectroscopy, two bands, B1g $= 112$ cm^{-1} and A1g $= 210$ cm^{-1} attributable to the SnO species, are observed, in addition to the signals related to the alumina substrate. This is in perfect agreement with the literature [50–55]. However, the typical band of SnO$_2$, centered at approximately 470 cm^{-1}, is not present (see Fig. 4). Nonetheless, this observation is in contrapositions by the XPS results, which is an extremely surface-sensitive technique, where the peaks of Sn 3d$_{5/2}$ at BE
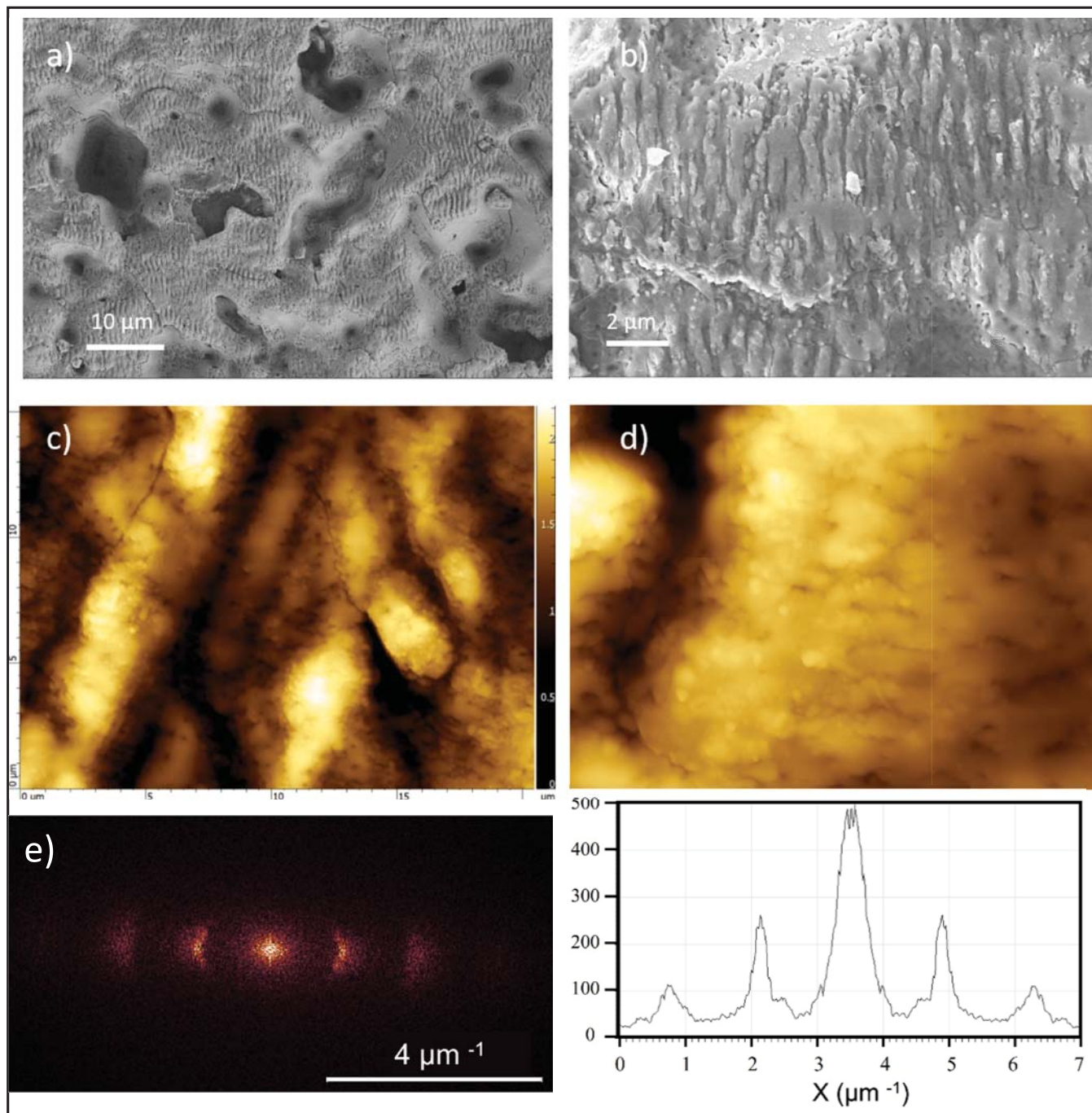
Table 2
AFM Roughness parameters: comparison between Ra and RMS and surface areas for bare alumina substrate and SnO-SnO$_2$ thin films as deposited and after fs-laser treatment.

	Bare Al$_2$O$_3$	SnO-SnO$_2$ as deposited	SnO-SnO$_2$ after fs-laser treatment
R$_a$ (nm)	62.3	67.6	272
RMS (nm)	78.1	85.2	303
Surface Area (μm^2)	231.9	247.1	284.1

Fig. 3. SEM micrographs (**a, b**) and AFM topographies (**c,d**) of SnO-SnO$_2$ films on Al$_2$O$_3$ substrate after fs-laser treatment at different magnifications. 2D-FFT transformation of a large area (45 μm x 65 μm) SEM image (**e**) and intensity signal profile (**f**).

= 486.6 eV and O 1 s at BE = 530.8 eV indicate the presence of Sn^{+4} oxidative state, corresponding to the SnO$_2$ upper coatings [27,56–59] (all the fitted photoemission peaks are shown in Fig. 5). Not only the XPS photoemission peaks, but also the valence band signal (see Fig. 6) confirms the presence of the SnO$_2$ surface termination showing the typical shape reported in the literature [59]. The main photoemission peaks, XPS at. % quantification, and corresponding chemical bonds of the thin film, both as deposited and after fs-laser treatment, are summarized in Table 3. The Sn/O ratio (both taking into account only −B signals) is 0.6. This suggests a slight deviation from the stoichiometric value of SnO$_2$, indicating an excess of Sn. This disproportion could arise from the presence of small quantities of SnO, which may generate crystal defects. From the Raman spectroscopy conducted on the fs-laser treated sample,

it emerges that there is no substantial modification of the structure after the laser treatment, as the observed peaks remain the same as those before the treatment. However, the signals appear narrower and more defined, suggesting that the laser treatment induces a more ordered and homogeneous recrystallization of the materials on the alumina substrate. On the other hand, XPS characterization highlights a decrease in the percentage of SnO$_2$ (from 20.9 at. % to 12.4 at. %) in favour of SnO (from negligible amount to 18.6 at. %). This is also evident from the shift and shape modification of the valence band spectra (Fig. 6), confirming that the laser treatment reduces the terminal part of SnO$_2$ present on the surface of the film [56–59], resulting in a more ordered structure as evidenced by Raman spectroscopy.

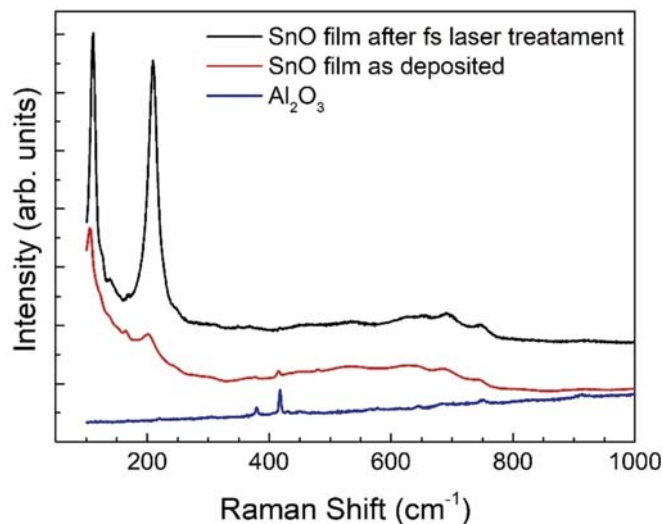Therefore, the complete compositional and structural study suggests

Fig. 4. Raman spectra of bare Al_2O_3 substrate, SnO-SnO_2 film as deposited and after fs-laser treatment.

the formation of a native SnO-SnO_2 structure, which can act as an active p-n junction at the interface due to the different electronic properties of the two materials. The fs-laser treatment induces a modification of the surface, by decreasing the quantity of SnO_2 species and forming a more complex SnO-SnO_2/SnO structure. As reported in previous studies, forming a p-n junction is an effective strategy to enhance the performance of chemiresistor gas sensors [10,25–27]. Specifically, the heterostructures formed between p-SnO and n-SnO_2 are crucial for improving gas sensing response at low temperatures compared to pure SnO_2 thin films. In fact, the junction of two materials with different work functions such as p-SnO and n-SnO_2 can create a region with an enhanced charge carrier density. This can lead to higher electron or hole mobility at low temperature, improving the sensitivity of the sensor to gases by decreasing the operating temperatures even at room temperature [60]. Moreover, the narrower valence band offsets of these heterojunctions reduce the energy required for electron transitions [26,27]. In other words, the charges present on the SnO-SnO_2 surface make these heterostructures more effective at attracting CO_2 gas than pure SnO_2 at room temperature.

The oxygen and the water molecules present in humid air interact with surface of the film forming ionized oxygen species (O^{2-}, O^-) and

hydroxyl ions, oxygen vacancies and electrons, respectively [61–63].

Exposing the SnO-SnO_2 to the CO_2 gas, it reacts with and the O^{2-} and hydroxyl species pre-adsorbed on film surface, releasing bicarbonate and carbonate ions, described in following chemical reactions (1), 2) [64]:

$$CO_2 + O^{2-} \rightarrow CO_3^{2-}(ads) \tag{1}$$

$$CO_2 + OH_{(ads)}^- \rightarrow HCO_3^-(ads) \tag{2}$$

Similar to pure SnO_2, this gas sensing mechanism leads to increase the device's resistance due to the reduction of accumulation layer hole concentration [60].

Furthermore, the SnO-SnO_2 p-n heterostructures show higher responses because, in addition to interacting with the chemisorbed oxygen, they can directly adsorb CO_2 molecules onto the surface by extracting electrons from the conduction band [26,27].

Concerning the effect of the laser treatment, it is possible to state that such formed p-n junction is compromised after the nanostructuring process, as XPS analysis shows a decrease in the presence of SnO_2 (see Table 3). The reduction of upper SnO_2 coating reduces the benefits offered by the heterostructure regarding sensitivity to CO_2 at room temperature, as will be described later in this paragraph. Nevertheless, the investigation of electrical material stability showed that the fs-laser treated film exhibits significantly higher stability compared to the untreated one. When left in the air for a day, it stabilizes at a consistent resistance value much faster than the untreated material, which shows more pronounced resistance fluctuations over the same period (see Fig. 7).

Once the sensor stabilized, sensitivity tests to CO_2 were conducted on the as-deposited sample. Initially, a calibration curve was generated and the sensor appears to respond linearly to the CO_2 concentrations in the range from 110 to 5000 ppm (Fig. 8) (In the range of values between 0 and 110 ppm, the gas response was not tested due to limitations in the experimental setup. Therefore, the linearly fitting calibration curve shown in Fig. 8 applies only to concentrations above 110 ppm). Outdoor CO_2 levels typically range from 350-400 ppm, while indoor environments typically aim for a maximum of 1500 ppm. Values exceeding 1500 ppm may lead to initial negative effects such as headaches, with significant health risks emerging around 5000 ppm, including nausea and increased heart rate [1]. The sensing response R (%) of the sensor was estimated by the equations (3) [60]:
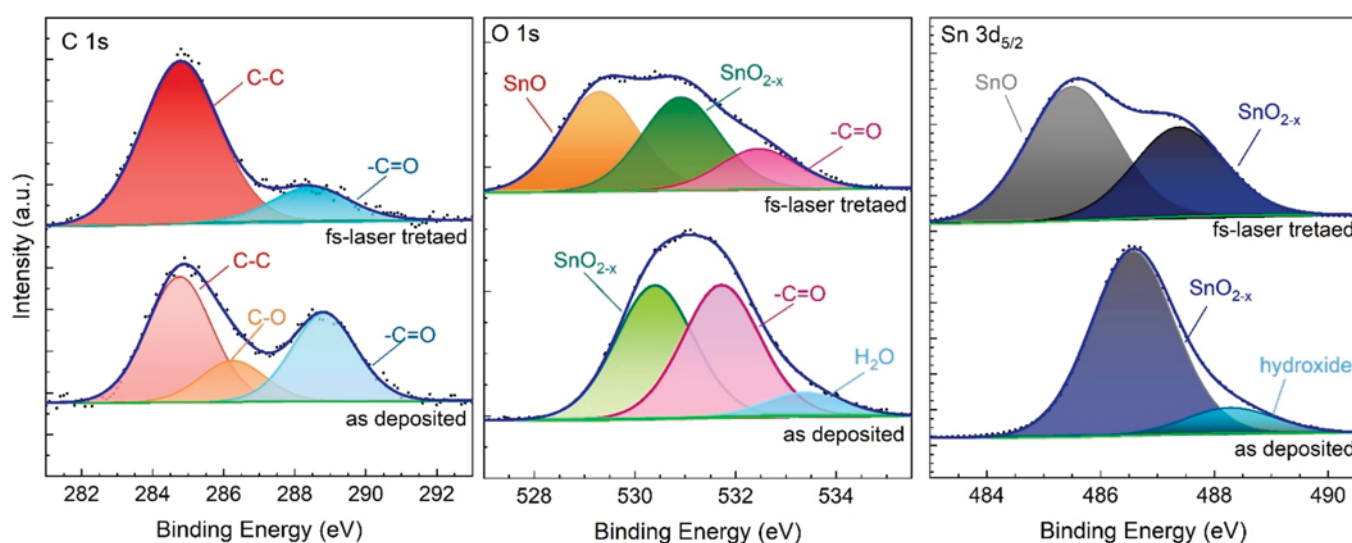

Fig. 5. Peak fitting of Sn 3d5, O 1 s, C1s of SnO-SnO_2 thin film as deposited and after fs-laser treatment.
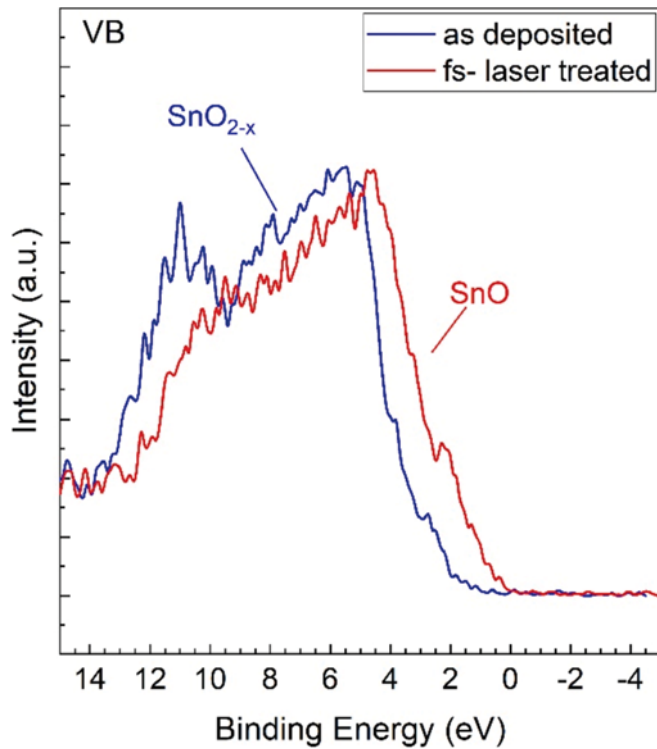
Fig. 6. Comparison of XPS valence band spectra of SnO- SnO$_2$ thin film as deposited and after fs-laser treatment.

Table 3
Main photoemission peaks, at. % quantification and corresponding chemical bond of SnO- SnO$_2$ thin film as deposited and after fs-laser treatment.

Peak	As deposited SnO- SnO$_2$			After fs-laser treatment		
	BE (eV)	At. %	Bond	BE (eV)	At. %	Bond
C1s − A	284.8	10.7	C-C	284.8	18.7	C-C
C1s − B	286.3	3.5	C-O	–		–
C1s − C	288.8	7.5	−C = O	288.4	3.9	−C = O
O1s − A	–			529.3	19.9	SnO
O1s − B	530.8	34.3	SnO$_{2-x}$	530.9	18.5	SnO$_{2-x}$
O1s − C	532.2	15.9	O chemiosorbed, OH groups, −C = O	532.5	8.0	O chemiosorbed, OH gropus, −C = O
O1s − D	533.4	4.1	H$_2$O	–	–	–
Sn3d5 − A	–	–	–	485.5	18.6	SnO
Sn3d5 − B	486.6	20.9	SnO$_{2-x}$	487.4	12.4	SnO$_{2-x}$ (nanostructured)
Sn3d5 − C	488.3	3.0	Sn hydroxide	–	–	–

$$R\,(\%) = \frac{(Rgas - Rair)}{Rair} \times 100 \tag{3}$$

Where the Rgas and Rair are the measured resistance before and after the CO$_2$ gas exposure. Regarding the sensitivity (S), it was estimated by the slope of the linear fitted curve of the sensing response, i.e. from equation (4) (see Fig. 8) [57,65]:

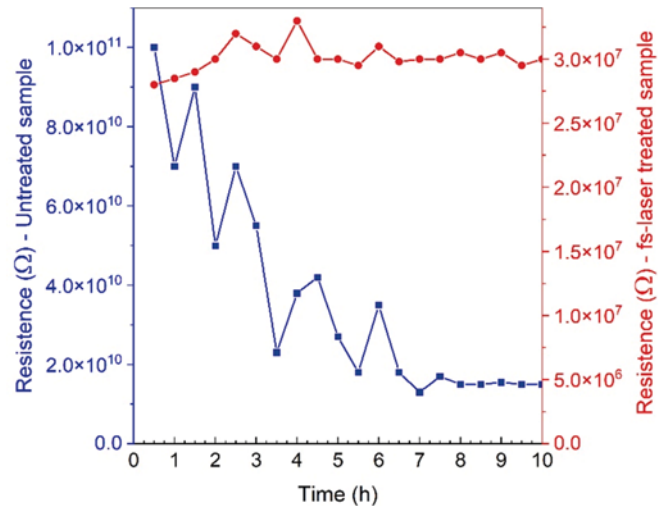$$R(\%) = S^*[CO_2] + Rair \tag{4}$$

Fig. 7. Comparison between electrical material stability for as deposited and fs-laser treated SnO-SnO$_2$ thin films.
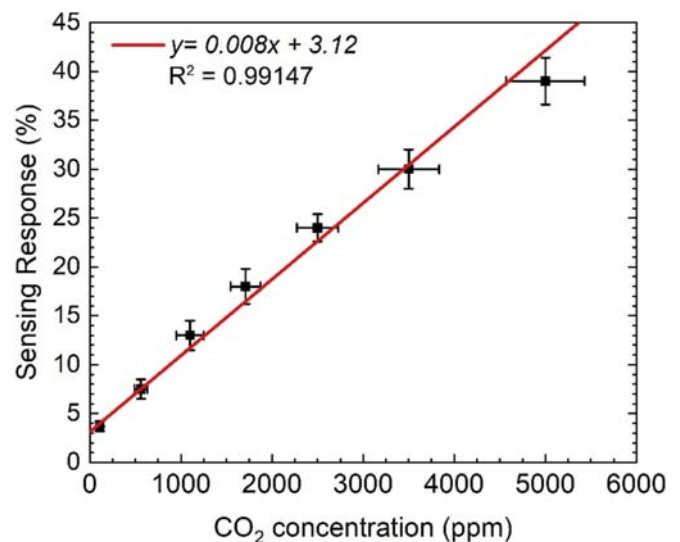

Fig. 8. Calibration curve in the range 110–5000 ppm of CO$_2$ concentration.

Where [CO$_2$] is the gas concentration.

The sensor demonstrates excellent sensing response within the concentration range of 1000 to 2000 ppm, showing R (%) levels ranging from 7 % to 20 %. Notably, R (%) increases to $\sim$ 40 % around the critical concentration of 5000 ppm (see Fig. 8). Therefore, the as-deposited gas sensors show highly sensitive response values, that can be attributed to the action of the p-n SnO-SnO$_2$ heterojunction formed natively with the e-beam deposition. Indeed, the evaluated sensitivity was found to be 0.008 %ppm^{-1}.

Then, multiple consecutive cycles were repeated at a CO$_2$ concentration of 5000 ppm. What is observed is that the sensitivity remains at high values even after some cycles Additionally, the sensor response time and recovery time were calculated to be about 1 s and 2 min, respectively (Fig. 9).

Conversely, the response of the femtosecond laser-treated sensor exhibits a peculiar behaviour that needed further investigation. It shows a "stepwise progression", meaning that the sensor's resistance value increases by the same amount for each cycle, never returning to its initial value. In other words, although the treated material displays a very short response time, the recovery time is infinite, meaning the sensor never returns to its initial conditions. Despite this, the resistance
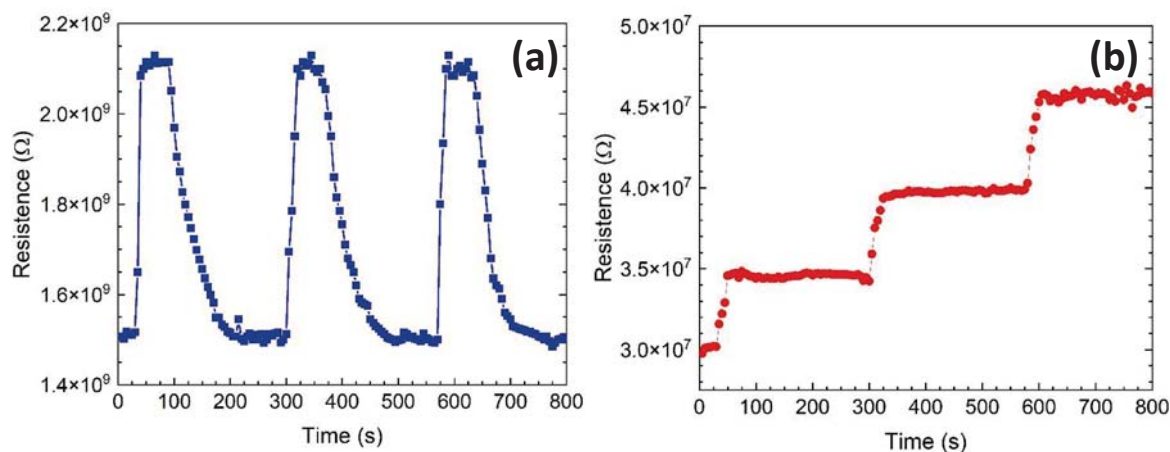
Fig. 9. Sensing response repeatability and recovery time characterization at 5000 ppm of CO_2 exposure for as deposited (a) and fs-laser treated (b) film.

increments for each cycle are constant, i.e., the resistance increases by a constant amount for each cycle. The difference in surface properties between the untreated and treated materials likely explains this phenomenon. A notable distinction lies in the presence of the non-stoichiometric n-type SnO_2 terminal layer, which is considerably less prevalent in the treated film in favour of the appearance of a more pronounced quantity of SnO reduced oxidation state. This hypothesis gains support from the spatial periodicity of the LIPSS, which corresponds to 780 nm, similar to the laser wavelength used for the fs-laser treatment (800 nm). This correspondence suggests a predominance of microstructured SnO covered by a thinner and inhomogeneous SnO_2 layer, which has however an active role in the gas detection. In fact, SnO interacts with the laser to produce structures with a periodicity that satisfies the condition $\Lambda = \lambda_{fs}$, as expected for metals and semiconductors with a narrow band gap such as SnO [49]. In contrast, if SnO_2 had been predominant, the treatment would have produced LIPSS at a high spatial frequency, with a periodicity $\Lambda \le \lambda_{fs}/2$, typical of wide bandgap semiconductors, as observed in a previous work by D. Scortitica et al. [66]. Consequently, the laser-treated material exhibits more p-type SnO behaviour, resulting in a lower value of the sensor's resistance before the gas exposure. Indeed, the equilibrium resistance value in air shifts from approximately $10^9 \, \Omega$ for the untreated (as-deposited) film to around $10^7 \, \Omega$ for the treated material, representing a starting value less than 100 times smaller.

When the surface of the fs-laser treated material interacts with CO_2, oxidation of SnO into SnO_2 may occur, initiating an irreversible chemical reaction and establishing a new equilibrium state with each CO_2 exposure cycle. This also explains why an increase of resistance was recorded when the sensor is exposed to the gas, as typically occurs for n-type materials. Over successive CO_2 cycles, the material's resistance will gradually increase until all oxygen vacancies on the surface are saturated.

Despite the irreversible changes induced by CO_2 on the treated film, multiple consecutive cycles were conducted to assess the sensor's sensitivity after numerous exposures to the gas. To facilitate this evaluation, the resistance R ratio value was calculated (Fig. 10). For the as-deposited film, it was simply computed as R/R_0, while it was the value of the step-by-step variation (i.e., R_n-cycle/R_{n-1} cycle) for the treated film.

By analyzing the slope of these plots, the cycle number at which the ratio becomes > 1.02 (considering 2 % as the detection limit of the signal with respect to the background) was extrapolated. This threshold indicates when the sensor remains sensitive to the gas. Through this approach, we could estimate that both sensors remain sensitive to the gas (R > 1.02) for more than 30 cycles. This indicates that both sensors exhibit the good sensitivity threshold, despite the treated sensor initially displaying lower sensitivity compared to the untreated sensor.
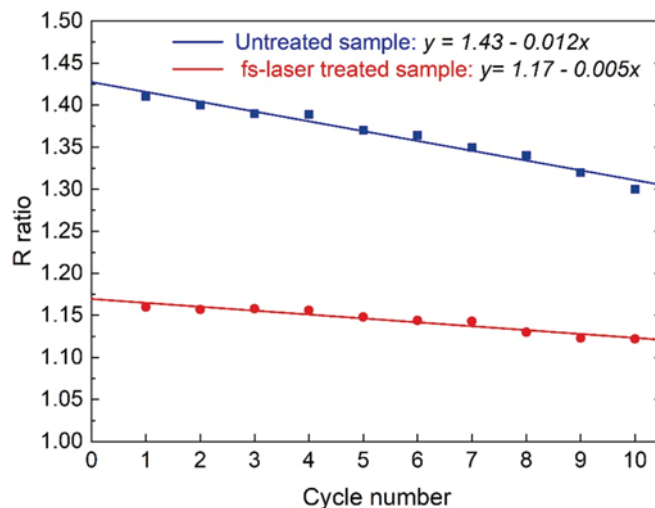

Fig. 10. R ratio value for as deposited (blue line) and fs-laser treated (red line) film.

Fig. 11 shows the different structures involved in the gas sensing mechanism. It seems reasonable to assume that before laser treatment, the sensor's primary mechanism is driven by the p-n heterojunction between SnO and SnO_2 which allow the sensor to operate at RT. After laser treatment, the main sensing role is played by the surface nanostructuring that enhances the surface area, active sites, and oxygen vacancies, improving CO_2 interaction. In this case, the sensing mechanism is different due the significantly reduced SnO_2 layer, with a response like a "stepwise progression" in the change of resistance, which is somewhat different for this kind of devices. Indeed, the presence of LIPSS could stimulate an enhanced sensing with the increased surface are, but, at the same time, trap the chemical species by getting unavailable the active sites for restoring the native surface. In any case, the fs-laser engineering and functionalization of the surface result in promising performance for the sensor in terms of signal stability, reproducibility, and RT operations.

These findings demonstrate the effectiveness of the SnO_2-based CO_2 sensor for real-world applications, particularly in promoting health and safety compliance in confined spaces with a high human occupancy or CO_2 production. Compared to Non-Dispersive Infrared (NDIR)-based commercial CO_2 sensors, the devices developed in this work are more stable in ambient condition, cost-effective and easily integrated into miniaturized systems, while maintaining comparable performance in
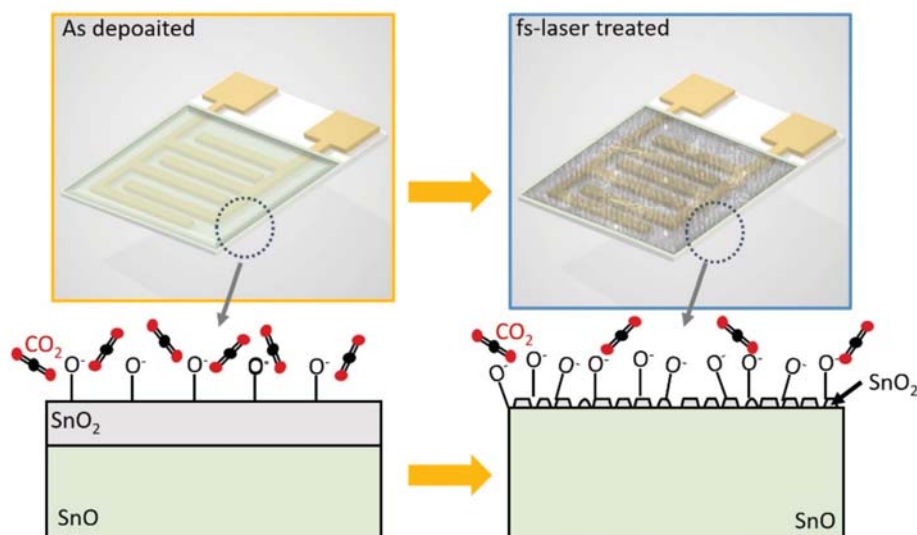
Fig. 11. Schematic illustration of gas sensing mechanism before and after the fs-laser treatment.

terms of sensitivity, recovery time, and device lifespan [67]. Operating efficiently at RT, the sensor shows significant potential for indoor air quality monitoring in smart building systems, HVAC (Heating, Ventilation, and Air Conditioning) systems, and environmental monitoring. Its energy-efficient operation, without the need for high-temperature activation, makes it ideal for homes, offices, and industrial spaces. This sensor can play a key role in IoT-based building management by collecting data on air quality, energy usage, and meteorological conditions. Such capabilities support real-time, cloud-based control of indoor environments, enhancing energy efficiency, comfort, and safety in both residential and commercial buildings.

4. Conclusions

The CO_2 sensing performance of SnO-SnO_2 heterojunctions formed by depositing thin films on alumina PCB with electron beam evaporation was tested at room temperature for both as-deposited and after fs-laser treated sensors. The untreated SnO-SnO_2 film showed a sensing response ranging from 7 % to 20 % for CO_2 concentrations of 1000 to 2000 ppm, and up to 40 % at the hazardous concentration of 5000 ppm. The formation of a p-n junction between SnO and SnO_2 significantly enhances the sensor's response. Despite the fs-laser modified the surface by improving the morphological features, as shown by SEM and AFM, the treated sensors did not show an improved response. However, they demonstrated good performance to detect CO_2 in terms of response stability, also showing a different behaviour in the gas sensing mechanism with respect to conventional MOX-based sensors. This could be exploited for specific applications in which a high stability and fast conditions to reach it are requested. Therefore, the fs-treatment represents a novel approach for modifying MOX gas sensor materials to operate effectively as fast sensor at room temperature, offering the potential for a standardized industrial process for their production.

CRediT authorship contribution statement

Eleonora Bolli: Writing – review & editing, Writing – original draft, Investigation, Formal analysis, Data curation, Conceptualization. **Alessandro Bellucci:** Writing – review & editing, Visualization, Investigation, Formal analysis, Data curation, Conceptualization. **Matteo Mastellone:** Writing – review & editing, Methodology, Formal analysis, Data curation. **Alessio Mezzi:** Writing – review & editing, Formal analysis, Data curation. **Stefano Orlando:** Writing – review & editing, Investigation. **Riccardo Polini:** Writing – review & editing,

Investigation, Formal analysis, Data curation. **Raffaella Salerno:** Writing – review & editing, Formal analysis, Data curation. **Antonio Santagata:** Writing – review & editing, Investigation. **Veronica Valentini:** Writing – review & editing, Investigation, Formal analysis, Data curation. **Daniele Maria Trucchi:** Writing – review & editing, Visualization, Validation, Supervision, Conceptualization.

Declaration of competing interest

The authors declare that they have no known competing financial interests or personal relationships that could have appeared to influence the work reported in this paper.

Acknowledgments

Data availability

Data will be made available on request.

References

[1] Who, Guidelines for Indoor Air Quality: Selected Pollutants Bonn, World Health Organization Regional Office for Europe, Germany, 2010.

[2] X. Ma, T. Zhang, C. Ji, Y. Zhai, X. Shen, J. Hong, Threats to human health and ecosystem: looking for air-pollution related damage since 1990, Renew. Sustain. Energy Rev. 145 (2021) 111146, https://doi.org/10.1016/j.rser.2021.111146.

[3] D. Fowler, P. Brimblecombe, J. Burrows, M. R. Heal, Peringe Grennfelt, D. S. Stevenson, A. Jowett, E. Nemitz, M. Coyle, X. Liu, Y. Chang, G. W. Fuller, M. A. Sutton, Z. Klimont, M. H. Unsworth and M. Vieno, A chronology of global air quality, Philos. Trans. A Math. Phys. Eng. Sci. 378 (2020), 2183, 10.1098/rsta.2019.0314.

[4] P. Kumar, A.B. Singh, T. Arora, S. Singh, R. Singh, Critical review on emerging health effects associated with the indoor air quality and its sustainable management, Sci. Total Environ. 872 (2023) 162163, https://doi.org/10.1016/j.scitotenv.2023.162163.

[5] H. Meixner, J. Gerblinger, U. Lampe, M. Fleischer, Thin-film gas sensors based on semiconducting metal oxides, Sens. Actuators B 23 (2–3) (1995) 119–125, https://doi.org/10.1016/0925-4005(94)01266-K.

[6] N. Yamazoe, G. Sakai, K. Shimanoe, Oxide Semiconductor Gas Sensors, Catal. Surv, Asia. 7 (2003) 63–75, https://doi.org/10.1023/A:1023436725457.

[7] G. Sberveglieri, Classical and novel techniques for the preparation of SnO_2, thin-film gas sensors, Sens. Actuators B 6 (1992) 239–247.

[8] S.W. Lee, P.P. Tsai, H. Chen, Comparison study of SnO_2 thin- and thick-film gas sensors, Sens. Actuators B 67 (2000) 122–127.

[9] B.K. Min, S.D. Choi, SnO_2 thin film gas sensor fabricated by ion beam deposition, Sens. Actuators B 98 (2004) 239–246.

[10] Y. Masuda, Recent advances in SnO_2 nanostructure based gas sensors, Sens. Actuators B 364 (2022) 131876.

[11] X. Tian, Z. Hu, C. Jia, H. Wang, X. Wei, A review of advanced gas sensor based on sputtering SnO_2 thin film challenges and opportunities, J. Environ. Chem. Eng 11 (2023) 111516.

[12] C. Zhang, K. Xu, K. Liu, J. Xu, Z. Zheng, Metal oxide resistive sensors for carbon dioxide detection, Coord. Chem. Rev. 472 (2022) 214758.

[13] C. Wang, L. Yin, L. Zhang, D. Xiang, R. Gao, Metal oxide gas sensors: sensitivity and influencing factors, Sensors (basel). 10 (3) (2010) 2088–2106, https://doi.org/10.3390/s100302088.

[14] S.J. Patil, A.V. Patil, C.G. Dighavkar, K.S. Thakare, R.Y. Borase, S.J. Nandre, N. G. Deshpande, R.R. Ahire, Semiconductor metal oxide compounds based gas sensors: A literature review, Front, Mater. Sci. 9 (2015) 14–37, https://doi.org/10.1007/s11706-015-0279-7.

[15] Y.G. Song, G.S. Kim, B.K. Ju, C.Y. Kang, Design of Semiconducting Gas Sensors for Room-Temperature Operation, J. Sens. Sci. Technol. 29 (1) (2020) 1–6.

[16] J. Zhang, X. Liu, G. Neri, N. Pinna, Nanostructured Materials for Room-Temperature Gas Sensors, Adv. Mater. 28 (2016) 795–831, https://doi.org/10.1002/adma.201503825.

[17] T.T. Zhou, T. Zhang, Recent Progress of Nanostructured Sensing Materials from 0D to 3D: Overview of Structure–Property-Application Relationship for Gas Sensors, Small Methods 5 (2021) 2100515, https://doi.org/10.1002/smtd.202100515.

[18] E. Bolli, A. Fornari, A. Bellucci, M. Mastellone, V. Valentini, A. Mezzi, R. Polini, A. Santagata, D.M. Trucchi, Room-Temperature O_3 Detection: Zero-Bias Sensors Based on ZnO Thin Films, Crystals 14 (2024) 90, https://doi.org/10.3390/cryst14010090.

[19] D. Wang, Y. Chen, Z. Liu, L. Li, C. Shi, H. Qin, J. Hu, CO2-sensing properties and mechanism of nano-SnO_2 thick-film sensor, Sens. Actuators B 227 (2016) 73–84.

[20] D. Degler, U. Weimar, N. Barsan, Current Understanding of the Fundamental Mechanisms of Doped and Loaded Semiconducting Metal-Oxide-Based Gas Sensing Materials, ACS Sensors 4 (2019) 2228–2249, https://doi.org/10.1021/acssensors.9b00975.

[21] M. Panday, G.K. Upadhyay, L.P. Purohit, Sb incorporated SnO2 nanostructured thin films for CO_2 gas sensing and humidity sensing applications, J. Alloys Compd. 904 (2022) 164053.

[22] V. Manikandan, I. Petrila, S. Vigneselvan, R.S. Mane, B. Vasile, R. Dharmavarapu, S. Lundgaard, S. Juodkazis, J. Chandrasekarang, A reliable chemiresistive sensor of nickel-doped tin oxide (Ni-SnO_2) for sensing carbon dioxide gas and humidity, RSC Adv. 10 (2020) 3796.

[23] B.Y. Song, C. Li, M.S. Lv, X.F. Zhang, G.L. Chen, Z.P. Deng, Y.M. Xu, L.H. Huo, S. Gao, Graphitic carbon-doped SnO_2 nanosheets-wrapped tubes for chemiresitive ppb-level nitric oxide sensors operated near room temperature, Sens. Actuators B. 374 (2023) 132822.

[24] J. Rodrigues, N.G. Shimpi, Indium doped SnO_2/polyaniline nanocomposites as a DMMP gas sensor at room temperature, Polym. Bull. (2024), https://doi.org/10.1007/s00289-023-05136-2.

[25] Z. Wang, P.K. Nayak, A. Albar, N. Wei, U. Schwingenschlögl, H.N. Alshareef, Transparent SnO–SnO2 p–n Junction Diodes for Electronic and Sensing Applications, Adv. Mater. Interfaces 2 (2015) 1500374, https://doi.org/10.1002/admi.201500374.

[26] H. Yua, T. Yanga, Z. Wangc, Z. Lia, Q. Zhaoa, M. Zhang, p-N heterostructural sensor with SnO-SnO2 for fast NO2 sensing response properties at room temperature, Sens. Actuators B. 258 (2018) 517–526.

[27] Z. Wang, F. Wang, A. Hermawan, Y. Asakura, T. Hasegawa, H. Kumagai, H. Kato, M. Kakihan, J. Zhu, S. Yin, SnO-SnO2 modified two-dimensional MXene $Ti_3C_2T_x$ for acetone gas sensor working at room temperature, J. Mater. Res. Technol. 73 (2021) 128–138.

[28] D. Wang, Y. Chen, Z. Liu, L. Li, C. Shi, H. Qin, J. Hu, CO2-sensing properties and mechanism of nano-SnO_2 thick-film sensor, Sens. Actuators B Chem. 227 (2016) 73–84.

[29] Y. Xiong, Q. Xue, C. Ling, W. Lu, D. Ding, L. Zhu, X. Li, Effective CO_2 detection based on LaOCl-doped SnO_2 nanofibers: Insight into the role of oxygen in carrier gas, Sens. Actuators B Chem. 241 (2017) 725–734.

[30] M.E. DMello, N.G. Sundaram, S.B. Kalidindi, Assembly of ZIF-67 metal-organic framework over tin oxide nanoparticles for synergistic chemiresistive CO_2 gas sensing, Chem. Eur. J. 24 (2018) 9220–9223.

[31] W. Zhang, C. Xie, G. Zhang, J. Zhang, S. Zhang, D. Zeng, Porous LaFeO3/SnO_2 nanocomposite film for CO_2 detection with high sensitivity, Mater. Chem. Phys. 186 (2017) 228–236.

[32] N. Rajesh, J.C. Kannan, T. Krishnakumar, A. Bonavita, S.G. Leonardi, G. Neri, Microwave irradiated Sn-substituted CdO nanostructures for enhanced CO_2 sensing, Ceram. Int. 41 (2015) 14766–14772.

[33] Y. Xiong, G. Zhang, S. Zhang, D. Zeng, C. Xie, Tin oxide thick film by doping rare earth for detecting traces of CO_2: Operating in oxygen-free atmosphere, Mater. Res. Bull. 52 (2014) 56–64.

[34] K.C. Hsu, T.H. Fang, Y.J. Hsiao, C.A. Chan, Highly responsive CO_2 gas sensor based on Au-La_2O_3 doped SnO_2 nanofibers, Mater. Lett. 261 (2020) 127144, https://doi.org/10.1016/j.matlet.2019.127144.

[35] S. Deepa, K. Prasanna Kumari, B. Thomas, Contribution of oxygen-vacancy defect-types in enhanced CO_2 sensing of nanoparticulate Zn-doped SnO_2 films, Ceram. Int. 43 (2017) 17128–17141, https://doi.org/10.1016/j.ceramint.2017.09.134.

[36] T. Iwata, K. Matsuda, K. Takahashi, K. Sawada, CO_2 sensing characteristics of a La_2O_3/SnO_2 stacked structure with micromachined hotplates, Sensors 17 (9) (2017) 2156, https://doi.org/10.3390/s17092156.

[37] C. Chaitra, H.M. Kalpana, C.M. Ananda, H.S. Lalithamba, Green synthesis of tin oxide-based nanoparticles using *Terminalia bellirica* seed extract: Impact of operating temperature and antimony dopant on sensitivity for carbon dioxide gas sensing application, Mater. Technol. (2022) 1–8, https://doi.org/10.1080/10667857.2022.2035143.

[38] Z.Y. Lee, H.F. Hawari, G.W. Djaswadi, K. Kamarudin, A highly sensitive room temperature CO_2 gas sensor based on SnO2-rGO hybrid composite, Materials 14 (2021) 522, https://doi.org/10.3390/ma14030522.

[39] M. Ehsani, M.N. Hamidon, A. Toudeshki, M.H.S. Abadi, S. Rezaeian, CO_2 gas sensing properties of screen-printed La_2O_3/SnO_2 thick film, IEEE Sens. J. 16 (2016) 6839–6845, https://doi.org/10.1109/JSEN.2016.2587779.

[40] H.M. van Driel, J.E. Sipe, J.F. Young, Laser-Induced Periodic Surface Structure on Solids: A Universal Phenomenon, Phys. Rev. Lett. 49 (1982) 26.

[41] M. Mastellone, A. Bellucci, M. Girolami, V. Serpente, R. Polini, S. Orlando, A. Santagata, E. Sani, F. Hitzel, D.M. Trucchi, Deep-Subwavelength 2D Periodic Surface Nanostructures on Diamond by Double-Pulse Femtosecond Laser Irradiation, Nano Lett. 21 (2021) 4477–4483.

[42] M. Mastellone, E. Bolli, V. Valentini, S. Orlando, A. Lettino, R. Polini, J. G. Buijnsters, A. Bellucci, D.M. Trucchi, Surface Nanotexturing of Boron-Doped Diamond Films by Ultrashort Laser Pulses, Micromachines 14 (2023) 389, https://doi.org/10.3390/mi14020389.

[43] P. Calvani, A. Bellucci, M. Girolami, S. Orlando, V. Valentini, R. Polini, D. M. Trucchi, Black diamond for solar energy conversion, Carbon 105 (2016) 401–407.

[44] J. Yong, F. Chen, Q. Yang, X. Hou, Femtosecond laser controlled wettability of solid surfaces, Soft Matter 11 (2015) 8897–8906, https://doi.org/10.1039/C5SM02153G.

[45] M. Mastellone, E. Bolli, V. Valentini, A. Bellucci, S. Orlando, A. Santagata, R. Polini, A. Lettino, E. Sani, D.M. Trucchi, Two-dimensional periodic surface nanotexturing of 6H-SiC by ultrashort laser pulses, Surfaces and Interfaces 46 (2024) 104006.

[46] A. Guarnaccio, C. Belviso, P. Montano, F. Toschi, S. Orlando, G. Ciaccio, S. Ferreri, D. Trevisan, D. Mollica, G.P. Parisi, P. Dolce, A. Bellucci, A. De Stefanis, D. M. Trucchi, V. Valentini, A. Santagata, F. Cavalcante, A. Lettino, L. Medici, P. P. Ragone, V.G. Lambertini, Femtosecond laser surface texturing of polypropylene copolymer for automotive paint applications, Surf. Coat. Technol. 406 (2021), https://doi.org/10.1016/j.surfcoat.2020.126727.

[47] J.M. Liu, Simple technique for measurements of pulsed Gaussian-beam spot sizes, Opt. Lett. 7 (1982) 196–198.

[48] V.E. Bochenkov, G.B. Sergeev, Sensitivity, Selectivity, and Stability of Gas-Sensitive Metal-Oxide Nanostructurea; American Scientific Publishers: Valencia, CA, USA, 2010; Volume 3, pp. 31–52. Available online: https://www.chem.msu.ru/rus/books/2011/sergeev/all.pdf.

[49] M. Mastellone, M.L. Pace, M. Curcio, N. Caggiano, A. De Bonis, R. Teghil, P. Dolce, D. Mollica, S. Orlando, A. Santagata, V. Serpente, A. Bellucci, M. Girolami, R. Polini, D.M. Trucchi, LIPSS Applied to Wide Bandgap Semiconductors and Dielectrics: Assessment and Future Perspectives, Materials 15 (2022) 1378, https://doi.org/10.3390/ma15041378.

[50] Y. Ogo, H. Hiramatsu, K. Nomura, H. Yanagi, T. Kamiya, M. Hirano, H. Hosono, P-channel thin-film transistor using p-type oxide semiconductor, SnO. Appl. Phys. Lett. 93 (3) (2008) 032113, https://doi.org/10.1063/1.2964197.

[51] J. Geurts, S. Rau, W. Richter, F.J. Schmitte, SnO films and their oxidation to SnO_2: Raman scattering, IR reflectivity and X-ray diffraction studies, Thin Solid Films 121 (1984) 217–225.

[52] J. Zuo, C. Xu, X. Liu, C. Wanga, C. Wang, Y. Hu, Y. Qian, Study of the Raman spectrum of nanometer SnO_2, J. Appl. Phys. 75 (1994) 1835.

[53] C. Meier, S. Lüttjohann, V.G. Kravets, H. Nienhaus, A. Lorke, P. Ifeacho, H. Wiggers, C. Schulz, M.K. Kennedy, F.E. Kruis, Vibrational and defect states on SnO_x nanoparticles, J. Appl. Phys. 99 (2006) 113108.

[54] D.M. Jang, H. Jung, N.D. Hoa, D. Kim, S.-K. Hong, H. Kim, Tin Oxide-Carbon Nanotube Composite for NOX Sensing, Journal of Nanoscience and Nanotechnology 12 (2012) 1425–1428.

[55] B. Eifert, M. Becker, C.T. Reindl, M. Giar, L. Zheng, A. Polity, Y. He, C. Heiliger, P. J. Klar, Raman studies of the intermediate tin-oxide phase, Phys. Rev. Mater. 1 (2017) 014602.

[56] C.K.G. Kwok, Y. Wang, X. Shu, K.M. Yu, Conversion of p-type SnO to n-type SnO_2 via oxidation and the band offset and rectification of an all-Tin oxide p-n junction structure, Appl. Surf. Sci. 627 (2023) 157295.

[57] M.U. Yousaf, E. Pervaiz, S. Minallah, M.J. Afzal, L. Honghong, M. Yang, Tin oxide quantum dots decorated graphitic carbon nitride for enhanced removal of organic components from water: Green process, Results in Physics 14 (2019) 102455.

[58] M. Epifani, S. Kaciulis, A. Mezzi, D. Altamura, C. Giannini, R. Díaz, C. Force, A. Genç, J. Arbiol, P. Siciliano, E. Comini, I. Concina, Inorganic Photocatalytic Enhancement: Activated RhB Photodegradation by Surface Modification of SnO2 Nanocrystals with V_2O_5-like species (supplementary info), Scientific Report 7 (2017) 44763.

[59] Avantage handbook.

[60] S. Keerthana, K. Rathnakannan, Room temperature operated carbon dioxide sensor based on silver doped zinc oxide/cupric oxide nanoflowers, Sens. Act. B Chem. 378 (2023) 133181, https://doi.org/10.1016/j.snb.2022.133181.

[61] X. Liu, M. Hu, Y. Wang, J. Liu, Y. Qin, High sensitivity NO_2 sensor based on CuO/p-porous silicon heterojunction at room temperature, J. Alloy. Compd. 685 (2016) 364–369, https://doi.org/10.1016/j.jallcom.2016.05.215.

[62] Y. Wang, F. Qu, J. Liu, Y. Wang, J. Zhou, S. Ruan, Enhanced H2S sensing characteristics of CuO-NiO core-shell microspheres sensors, Sens. Actuators, B Chem. 209 (2015) 515–523, https://doi.org/10.1016/j.snb.2014.12.010.

[63] Z. Bai, C. Xie, M. Hu, S. Zhang, D. Zeng, Effect of humidity on the gas sensing property of the tetrapod-shaped ZnO nanopowder sensor, Mater. Sci. Eng. B 149 (2008) 12–17, https://doi.org/10.1016/j.mseb.2007.11.020.

[64] D.A. Parkes, Oxygen negative ion reactions with carbon dioxide and carbon monoxide Part 1, J. Chem. Soc. Faraday Trans. 1 Phys. Chem. Condens. Phases, 68 (1972), 627-640, 10.1039/F19726800627.

[65] K. Rathi, K. Pal, Wireless Hand-Held Device Based on Polylactic Acid-Protected, Highly Stable, CTAB-Functionalized Phosphorene for CO_2 Gas Sensing, ACS Appl. Mater. Interfaces 12 (34) (2020) 38365–38375.

[66] D. Scorticati, A. Illiberi, G.R.B.E. Römer, T. Bor, W. Ogieglo, M. Klein Gunnewiek, A. Lenferink, C. Otto, J.Z.P. Skolski, F. Grob, D.F. de Lange, A.j., Huis in 't Velda, Optical and electrical properties of SnO_2 thin films after ultra-short pulsed laser annealing, Laser Material Processing for Solar Energy Devices II, SPIE (2013) 64–75.

[67] T.-P. Teng, W.-J. Chen, A compensation model for an NDIR-based CO_2 sensor and its energy implication on demand control ventilation in a hot and humid climate, Energy and Buildings 281 (2023) 112738, https://doi.org/10.1016/j.enbuild.2022.112738.